Highlights

- Computational modeling of retinal cells from connectomes of a healthy and a degenerated retina
- Simulations represent the current flow from rod photoreceptors to rod bipolar cells (RodBCs)
- Photocurrent input leads to lower membrane potential at degenerated RodBCs than healthy RodBCs
- Despite altered morphologies, loss of rod inputs is the main reason for lower membrane potentials
- Frequency response exhibit similar low pass filter effect for both healthy and degenerated RodBCs

Title: Model-based Comparison of Current Flow in Rod Bipolar Cells of Healthy and Early-Stage Degenerated Retina

Authors: Pragya Kosta[1*], Ege Iseri[2], Kyle Loizos[3], Javad Paknahad[4], Rebecca L. Pfeiffer[5], Crystal L. Sigulinsky[5], James R. Anderson[5], Bryan W. Jones[5*], Gianluca Lazzi[2,3,4,6*]

Affiliations:

[1]Department of Electrical and Computer Engineering, University of Utah, Salt Lake City, UT

[2]Department of Biomedical Engineering, University of Southern California, Los Angeles, CA

[3]Institute for Technology and Medical Systems (ITEMS), Keck School of Medicine, University of Southern California, Los Angeles, CA

[4]Department of Electrical Engineering, University of Southern California, Los Angeles, CA

[5]John Moran Eye Center at the University of Utah, Salt Lake City, UT

[6]Departments of Ophthalmology and Clinical Entrepreneurship, University of Southern California, Los Angeles, CA

*****Correspondence to: Pragya.kosta@utah.edu or bryan.jones@m.cc.utah.edu or lazzi@usc.edu

Abstract

Retinal degenerative diseases, such as retinitis pigmentosa, are generally thought to initiate with the loss of photoreceptors, though recent work suggests that plasticity and remodeling occurs prior to photoreceptor cell loss. This degeneration subsequently leads to death of other retinal neurons, creating functional alterations and extensive remodeling of retinal networks. Retinal prosthetic devices stimulate the surviving retinal cells by applying external current using implanted electrodes. Although these devices restore partial vision, the quality of restored vision is limited. Further knowledge about the precise changes in degenerated retina as the disease progresses is essential to understand how current flows in retinas undergoing degenerative disease and to improve the performance of retinal prostheses. We developed computational models that describe current flow from rod photoreceptors to rod bipolar cells (RodBCs) in the healthy and early-stage degenerated retina. Morphologically accurate models of retinal cells with their synapses are constructed based on retinal connectome datasets, created using serial section transmission electron microscopy (TEM) images of 70 nm-thick slices of either healthy (RC1) or early-stage degenerated (RPC1) rabbit retina. The passive membrane and active ion currents of each cell are implemented using conductance-based models in the Neuron simulation environment. In response to photocurrent input at rod photoreceptors, the simulated membrane potential at RodBCs in early degenerate tissue is approximately 10-20 mV lower than that of RodBCs of that observed in wild type retina. Results presented here suggest that although RodBCs in RPC1 show early, altered morphology compared to RC1, the lower membrane potential is primarily a consequence of reduced rod photoreceptor input to RodBCs in the degenerated retina. Frequency response and step input analyses suggest that individual cell responses of RodBCs in either healthy or early-degenerated retina, prior to substantial photoreceptor cell loss, do not differ significantly.

Keywords

Degenerated Retina
Rod Bipolar Cells
Rod Pathways
Computational Modeling
Neuronal Modeling
Retinal Degeneration
Retinitis Pigmentosa
Neurodegeneration

1. Introduction

Signal processing through retinal circuitry allows for propagation of visual primitives out of the eye to the cortex for visual perception. Retinal bipolar cells collect postsynaptic output from photoreceptors and transfer processed information to horizontal, amacrine and ganglion cells [Kolb, 2003, Bloomfield, et al., 2001]. While amacrine cell processes remain within the retina, the axons of ganglion cells form the optic nerve carrying the visual primitives to other areas in the brain for further processing. Retinal degenerative diseases, such as retinitis pigmentosa (RP) or age-related macular degeneration (AMD), cause progressive damage to the retina. The retinal degeneration initiates numerous retinal remodeling processes that affect both neurons and glia [Pfeiffer, et al., 2020a]. In the early phases of degeneration, photoreceptors exhibit hallmarks of cellular stress, followed by photoreceptor cellular death. As the disease progresses and photoreceptors are lost, extensive remodeling of retinal networks occurs. It has been hypothesized that the absence of presynaptic signals from photoreceptors results in morphological as well as circuit and functional alterations in the surviving cells [Marc, et al., 2007, Jones, et al., 2013, Pfeiffer, et al., 2020b]. A primary component of retinal remodeling is the process of rewiring, where aberrant processes (neurites) grow from dendrites, axons, and somas of surviving neurons [Jones, et al., 2013]. Functionally, following the complete loss of photoreceptor inputs, an oscillatory behavior has been observed in degenerate retina that leads to spontaneous spiking of ganglion cells [Trenholm, et al., 2015, Ivanova, et al., 2016]. In the later phases of degeneration, physical relocation of surviving neuron somas, and topological restructuring of dendrites and axons occurs, along with improper connectivity, eventually leading to extensive neuronal death and subsequent total vision loss.

Visual prosthetic systems have been developed to treat retinal degenerative diseases, including AMD and RP [Weiland, et al., 2014, Farnum, et al., 2020]. While cortical implant based visual prosthetic systems, which bypass the retina completely and directly stimulate the visual cortex, could be useful in the case of several types of vision diseases, these systems are still under development [Farnum, et al., 2020, Niketeghad, et al., 2019, Kosta, et al., 2018, Troyk, 2017, Fernandez, et al., 2017, Lowery, et al., 2017] and the principles of how to encode visual information that would mimic ganglion cell activity are unclear. In contrast, retinal implant based prosthetic systems aim to stimulate the surviving retinal circuitry by applying external current via implanted electrodes, utilizing the existing ganglion cell connections and outputs to the central nervous system, as well as other nuclei involved in vision and paravisual functions. Multiple epiretinal prosthetic systems have passed clinical trials and were shown to be effective in restoring useful vision [Ahuja, et al., 2013, Ayton, et al., 2014]. However, the quality of restored vision is limited and not comparable to the percepts achieved by a healthy retina. There are a number of proposed solutions, but improving the performance of retinal prostheses, relies on further knowledge about precisely what changes within the circuitry and how current flows in the retina as disease progresses.

Several computational modeling approaches have been employed to better understand retina function and interaction with prosthetics [Guo, et al., 2014]. Single-compartment conductance-based models have been created for different classes of retinal cells [Usui, et al., 1996, Publio, et al., 2009, Fohlmeister, et al., 2010]. These models simulate the biophysics of cells using equivalent electrical circuits and are designed to reproduce the results obtained from electrophysiological recordings of retina. Other studies have employed continuum medium models based on the effective medium properties of the neural population, ignoring individual

Abbreviations: Rod bipolar cell (RodBC); Retinal connectome 1 (RC1); Retinal pathoconnectome 1 (RPC1); Rod bipolar cells of RC1 (RC1-RodBC); Rod bipolar cells of RPC1 (RPC1-RodBC) cells [Abramian, et al., 2014]. Yet another modeling approach is to build abstractions of retinal circuitry including nonuniform sampling and adaptation [Shah, et al., 1996]. Although these modeling approaches help provide useful insights, most of these studies either use single-compartment models or artificial cell morphologies. However, it has been shown that morphology plays a critical role in the functional behavior of a cell and its network. For example, ganglion cells with distinct dendritic types perform specific functions important in model accuracy [Guo, et al., 2013]. The primary challenge in building a model with morphological details is the sparse availability of the morphology of retinal cells within the greater context of knowing the precise retinal neural network topology.

Further, multi-scale modeling strategies have been used by our group and others [Guo, et al., 2014, Loizos, et al., 2014, Loizos, et al., 2018, Stang, et al., 2019, Kosta, et al., 2020, Paknahad, et al., 2020a, Paknahad, et al., 2020b] to computationally model the vertebrate retina and its behavior in the presence of electrical stimulation. In our past work, we created a multi-scale model for retinal stimulation via a multi-electrode array, using cell morphologies and synaptic information from a retinal connectome of a healthy rabbit retina [Loizos, et al., 2018]. To replicate the degenerated retina more closely, several disease-related physiological and anatomical features were included in the model, such as reducing the thickness of various retinal layers and adding local feedback circuits between amacrine cells and cone bipolar cells (ConeBCs) to incorporate the spontaneous activity as observed in the degenerated retina [Loizos, et al., 2018]. Even though the model was artificially revised to mimic behavior of degenerated retina, it primarily relied on cell morphologies and synaptic connections based on a connectome database of a healthy retina.

With the help of retinal connectomics approaches, we have the opportunity to build morphologically and topologically realistic models of normal retinal networks [Anderson, et al., 2011a, Marc, et al., 2013], as well as diseased retinal networks [Pfeiffer, et al., 2020b, Pfeiffer, et al., 2020c]. Retinal connectomes are generated by sectioning the retina tissue in 70 nm-thick (or thinner) slices, capturing high-resolution images (2 nm/pixel) of each slice, annotating all cells and their synaptic connections, and then rendering a 3D reconstruction of these annotations across all slices along with diagrams describing network topologies [Marc, et al., 2013]. Such models based on measured morphology and quantification of synapses extracted from the connectome of actual diseased retina are highly valuable to modeling efforts. The understanding of the functional changes in the degenerated retina through accurate models of retinal cells and network can significantly impact the development of the next generation of retinal treatments and prosthetics. Our ultimate goals are to combine the detailed neural network model of degenerated retina with a bulk retina tissue model to analyze current flow through complete models of retina, as well as model the interaction of the retina with prosthetic electrodes by computing fields generated by electrodes. These models will not only provide a tool to understand various features of retinal networks, but they will serve as the most realistic tool available for analyzing and designing retinal prosthetic devices by investigating the retinal response to various stimulation paradigms, such as different stimulus waveforms and electrode designs.

In this work, we develop computational models to study changes in signal processing in early-stage degenerate retina with respect to healthy retina. Specifically, using our recently developed connectome of early-stage degenerated retina (RPC1) [Pfeiffer, et al., 2020b, Pfeiffer, et al., 2020c] and previous connectome of healthy retina (RC1) [Marc, et al., 2013], we built separate computational models of the current flow at the first visual synapse, from rod photoreceptors to rod bipolar cells (RodBCs), of the healthy (RC1-RodBCs) and degenerated retina (RPC1-RodBCs), and analyzed the individual RodBC responses. We created morphologically accurate models of RodBCs and used conductance-based modified Hodgkin-Huxley models [Hodgkin, et al., 1952] and cable theory to implement the biophysical behavior of retinal cells in the Neuron simulation environment [Hines, et al., 1997]. Passive cell membranes and active ionic currents are represented by equivalent electrical circuits and equations, which are solved at every time step of the simulation. We used a mathematical model of photocurrent injection to represent the light stimulus and transduction of light at rod photoreceptors. We leveraged the developed models to analyze the responses of RPC1-RodBCs to photocurrent input and compare against that of RC1-RodBCs. Additionally, we examined differences in RPC1-RodBCs and RC1-RodBCs with respect to step input and frequency response.

2. Retinal Connectomics

Synaptic level connectomics approaches are designed to capture the complete network graph representation of the neural network of a region of neural tissue. These graphs are constructed with the help of ultrastructural imaging techniques, image processing algorithms, data assembly, classification theory, and graph theory [Marc, et al., 2013]. The retinal tissue in these connectomes and pathoconnectomes (connectomes of pathological tissues) derives from serial 70 nm-thick slices, captured with high-resolution transmission electron microscopy (TEM) imaging approaches. The magnified images of tissue slices are then manually annotated for sizes and locations of various types of cells, recording the morphology of the cells and identifying their subcellular components (such as pre- and postsynaptic densities, ribbon synapses, gap junctions). These annotations are stored in a large-scale database, and specific data of a cell, synapse, or network across all the slices are extracted with the help of data mining tools, such as Viking Viewer [Anderson, et al., 2011b], CellSketches, Tulip [Auber, 2010], or Graffinity [Kerzner, et al., 2017]. These approaches provide the real cell morphology, network topology, and exact quantification of the location, number and size of synapses.

We are using a connectome of a healthy rabbit retina (RC1) [Anderson, et al., 2011a, Marc, et al., 2013] as a control. Retinal cells, including different types of bipolar cells, amacrine cells, and ganglion cells, are annotated, and synaptic connections between cells are quantified. To observe the changes in the retina with the progression of degenerative disease, we are developing connectomes of pathological tissues of four stages of degeneration [Pfeiffer, et al., 2019, Pfeiffer, et al., 2020c]. The first pathoconnectome (RPC1) is developed using an early-stage degenerated ten month-old transgenic (Tg) P347L rabbit retina model of RP [Pfeiffer, et al., 2020b, Pfeiffer, et al., 2020c]. In the selected region of the retina, the thickness of the outer plexiform layer is found to be reduced by approximately 50%. The degeneration of rod photoreceptors is initiated, though many are found to be intact. RodBCs extend neurites to the terminals of cone photoreceptors as the rod photoreceptors degenerate [Pfeiffer et al., 2020b, Cuenca, et al., 2004, Peng, et al., 2000]. Further, abnormal network connections between all RodBCs and AII glycinergic amacrine cells are observed in RPC1 [Pfeiffer, et al., 2020b]. As we continue to construct connectomes of the next stages of degeneration, we plan to computationally model the networks of various stages of the degenerated retina. In this manuscript, we focus on computational modeling and comparison of RodBCs of RC1 and RPC1 to capture early changes that could potentially shed light on the possibility of developing early treatment strategies, prior to substantial cone photoreceptor cell and bipolar cell loss.

3. Models and Methods

3.1 Data Extraction

To build the computational model, we extracted the morphology and topology data of RodBCs from RC1 and RPC1 connectomes. Custom Python scripts, along with Tulip [Auber, 2010] and vaa3D software [Peng, et al., 2014], were used for data extraction, visualization, and interpretation. For neuronal modeling, the extracted morphology data was post-processed in order to make it compatible with the Neuron software environment [Hines, et al., 1997]. The morphology of each cell is represented as a graph and refined such that there is not more than one root node and no separate sub-graphs. Therefore, broken edges between sub-graphs that occur due to missing annotations are bridged with the help of custom MATLAB scripts. Then, refined morphologies are converted in SWC format and imported in the Neuron simulation environment for simulations.

The RPC1 connectome contains 17 annotated RodBCs; however, only 8 have axonal and dendritic arbors contained entirely within the connectome volume. We compared these 8 RPC1-RodBCs (with Cell IDs 822, 933, 1001, 1069, 1232, 1243, 1537, and 25001 of RPC1 data) against 4 RC1-RodBCs (with Cell IDs 519, 5017, 7054, and 8749 of RC1 data). Fig 1 presents the morphology of these cells, with somas in blue, dendrites in black, axons in yellow, and axon terminals in red color. Some of the RPC1-RodBCs have abnormally longer branches in their axonal arbors compared to RC1-RodBCs. Next, the synapses between these RodBCs and rod photoreceptors are extracted from the connectomes. The RC1 connectome does not contain the outer plexiform layer, and therefore, the RodBC dendritic arbors and rod photoreceptor inputs are not present. To complete the cell morphology of RC1-RodBCs, we have patched the cells using RPC1-RodBC dendrites that were the most similar in morphology to those seen in healthy retina. To mimic the case of a healthy retina, there are 30 rod photoreceptors connected to each grafted dendritic arbor [Behrens, et al., 2016, Tsukamoto, et al., 2013]. The synaptic locations of the rod photoreceptor inputs are randomly selected, and we verified that the locations of these synapses do not have a significant impact on the response of RC1-RodBCs (see Section 4.1.1).

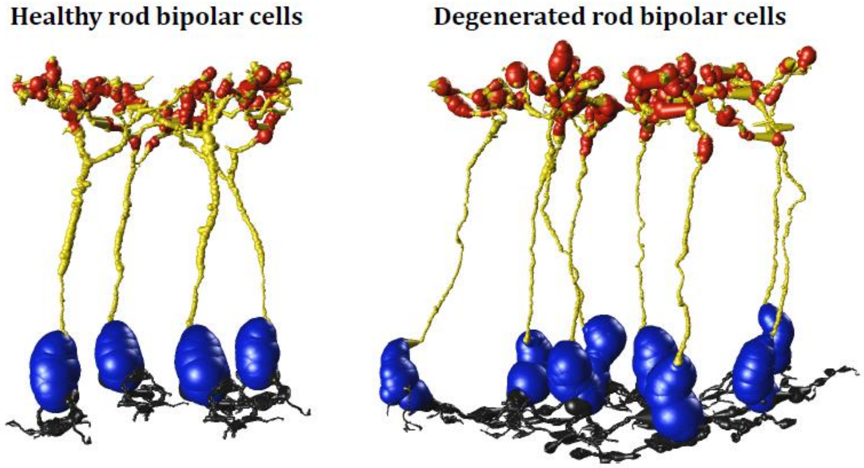

Figure 1: Morphology of healthy (left) and degenerated (right) RodBCs, extracted from RC1 and RPC1, respectively. Cell somas are depicted in blue, dendrites in black, axons in yellow and axon terminals in red color.

3.2 Rod Photoreceptor Model

The rod photoreceptors are modeled using a single-compartment model with passive membrane properties and voltage-gated ion channels based on [Kamiyama, et al., 1996, Publio, et al., 2006]. An intracellular calcium concentration system is implemented as in [Usui, et al., 1996] in order to model the calcium-dependent currents. The following six ionic currents are included in the model: hyperpolarization activated current (I_h), non-inactivating potassium current (I_{Kx}), delayed rectifying potassium current (I_{Kv}), calcium current (I_{Ca}), calcium-dependent chloride current ($I_{Cl(Ca)}$) and calcium-dependent potassium current ($I_{K(Ca)}$). The equivalent electrical circuit of the model is given by the following equation:

$$C_m \frac{dV}{dt} = -\left(I_{leak} + I_h + I_{Kx} + I_{Kv} + I_{Ca} + I_{Cl(Ca)} + I_{K(Ca)}\right) \tag{1}$$

where C_m is the membrane capacitance, and I_{leak} is the passive membrane current. The ion currents are implemented by Hodgkin–Huxley equations based on conductance, gating variables, and reversal potentials [Hodgkin, et al., 1952]. These model parameters are tuned (Table 1 of the appendix) such that the model replicates the experimental recording of rod photoreceptors closely.

The phototransduction process is represented by the application of photocurrent stimulus to the rod photoreceptors [Publio, et al., 2006]. The dark current of -40 pA is considered, and the simulated photocurrent is applied at the soma. The total photocurrent and the corresponding membrane potential at the soma of the photoreceptor are computed and presented in Fig 2(a) and Fig 2(b), respectively. With an increase in the amplitude of photocurrent, the hyperpolarization of the rod photoreceptor increases. As the photoreceptor models are single-compartment and identical, the membrane potential is the same for each rod photoreceptor. Even though the details of phototransduction at the outer segments of the rod photoreceptors are omitted, this simple model successfully provides the membrane potentials and currents. The simulated membrane potential at the rod photoreceptors is similar to that of experimental recordings [Kamiyama, et al., 1996, Kourennyi, et al., 2004].

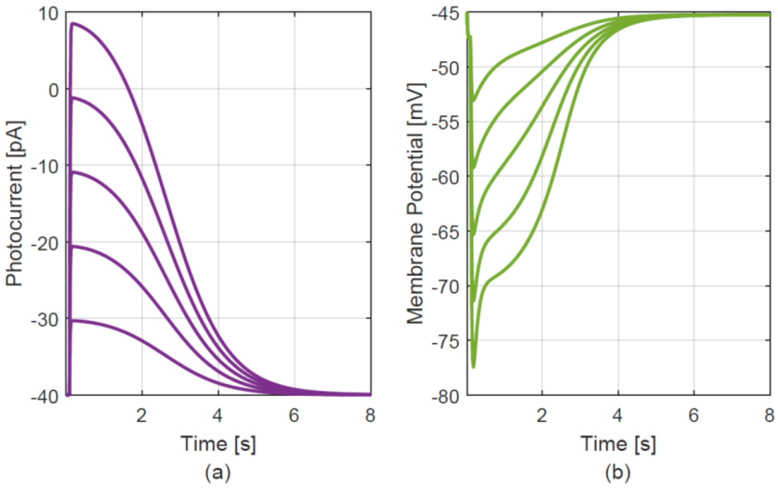

Figure 2: Simulated response of rod photoreceptor. Panel (a) presents simulated photocurrent waveforms with various current amplitudes and panel (b) displays the resulting membrane potential at the soma of rod photoreceptor corresponding to the photocurrents of panel (a).

3.3 RodBC Model

Morphologically-detailed RodBCs are implemented using multi-compartment models. The exact 3D structure of cell somas, dendrites, axons, and axon terminals are extracted from RC1 and RPC1. The compartmentalized model is implemented using cable theory, and each compartment is represented by a tapered cylinder, with radii and length computed using cell morphology. The biophysical behavior of RodBCs is modeled using a conductance-based model with passive membrane and five ionic currents [Publio, et al., 2009, Usui, et al., 1996]: voltage-dependent potassium current (I_{Kv}), calcium-dependent potassium current ($I_{K(Ca)}$), calcium current (I_{Ca}), hyperpolarization-activated current (I_h), and transient outward current (I_A). The following equation represents the equivalent electrical circuit of the cell membrane:

$$C_m \frac{dV}{dt} = -\left(I_{leak} + I_h + I_{Kv} + I_A + I_{Ca} + I_{K(Ca)}\right) \tag{2}$$

The ionic currents are implemented using modified Hodgkin–Huxley equations, and the model parameters are tuned to replicate the results from experimental recordings [Oltedal, et al., 2009]. To validate the model, depolarizing and hyperpolarizing VClamp inputs of ±20 mV (with resting potential of -70 mV) are applied at the soma of RC1-RodBCs. The resulting membrane current is simulated and found similar to the electrophysiological recordings of [Oltedal, et al., 2009]. The maximum conductances and reversal potentials of ion channels are provided in Table 1 of the appendix.

3.4 Rod Photoreceptor - RodBC Synapse Model

A mathematical model represents the graded chemical synapse between rod photoreceptors and RodBCs based on the synapse model of [Publio, et al., 2009] and [Mulloney, 2003]. The synaptic current is computed from the presynaptic voltage and then injected in the postsynaptic neuron. The synaptic current is given by:

$$I_{syn}(t) = g_{max}\, S(t)\left(V(t) - E_{syn}\right) \tag{3}$$

where g_{max} is maximum conductance, E_{syn} is reversal potential and $S(t)$ determines the activation level of a synapse depending on presynaptic voltage values [Publio, et al., 2009, Sikora, et al., 2005] and given by:

$$\frac{dS(t)}{dt} = \frac{S_\infty - S(t)}{(1 - S_\infty)\, \tau\, S(t)} \tag{4}$$

$$S_\infty = \begin{cases} \tanh\left(\frac{V_{pre} - V_{th}}{V_{slope}}\right), & if\ V_{pre} \geq V_{th} \\ 0, & otherwise \end{cases} \tag{5}$$

where τ defines the time constant of synapse activation, V_{pre} is presynaptic voltage, V_{slope} modulates the course of synapse activation, and V_{th} is the threshold voltage of synapse activation. When V_{pre} crosses V_{th}, synapse activation begins, and synaptic current starts flowing from presynaptic cell to postsynaptic cell. As the chemical synapse numbers (ribbon synapses, postsynaptic densities) are not changed at this stage of degeneration [Pfeiffer, et al., 2020b], the same synapse properties are used in both healthy and degenerated models. Table 2 of the appendix presents the parameters of the synapse model.

Next, the current flow from rod photoreceptors to RodBCs is simulated. The simulated photocurrent is injected into rod photoreceptors, and the resulting membrane potential is computed. Based on presynaptic voltage, current flow from rod photoreceptors to RodBCs via chemical synapses is simulated. The resulting membrane potential in the RodBC is computed at the soma and distant axon terminal of cells from both healthy and degenerated retinas. The computed membrane potential response of the RC1-RodBCs due to photocurrent input is found to be consistent with other works [Usui, et al., 1996, Trexler, et al., 2005, Cho, et al., 2016].

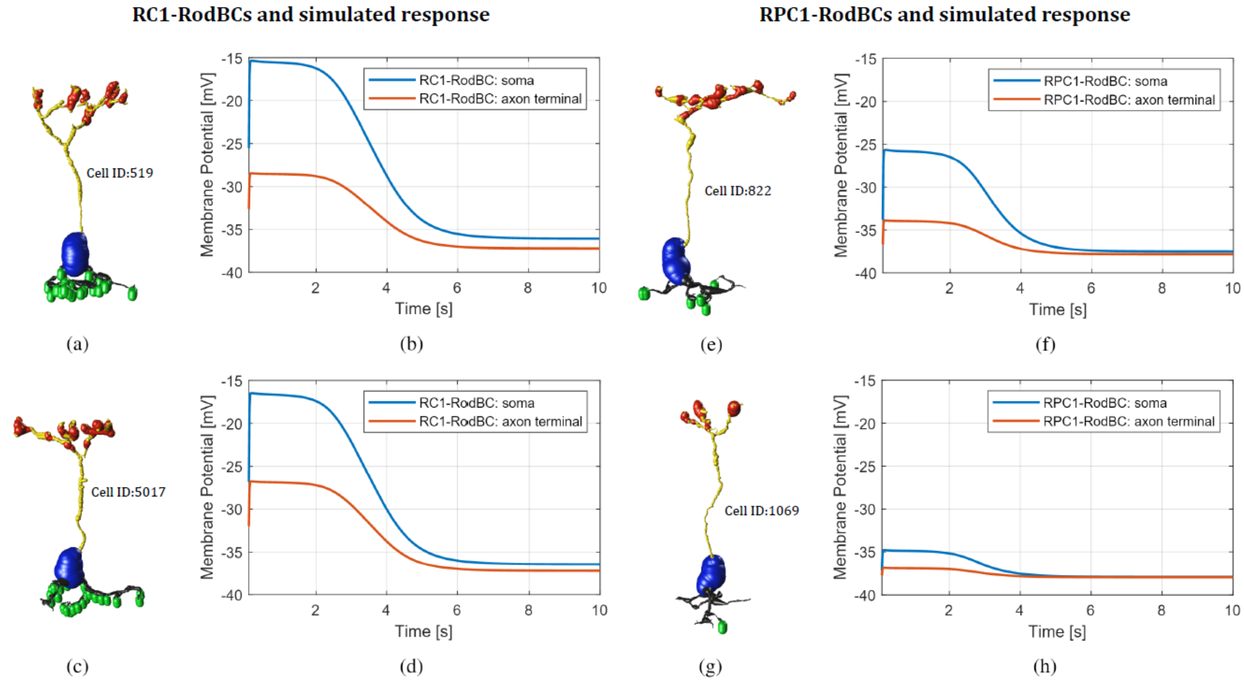

Figure 3: Simulated response of RC1-RodBCs vs. RPC1-RodBCs. Panel (a)-(d) correspond to two RC1-RodBCs (Cell IDs: 519 and 5017), whereas panel (e)-(h) correspond to two RPC1-RodBCs (Cell IDs: 822 and 1069). Locations and number of rod photoreceptor inputs for each RodBC are shown by green color. Panel (b), (d), (f) and (h) present the membrane potential at the somas and distant axon terminals of the RodBCs shown in panel (a), (c), (e) and (g), respectively.

4. Results

After validating the models of current flow from rod photoreceptors to RodBCs, we performed studies to analyze the differences between RodBCs of the healthy and early-stage degenerated retinas. First, we compared the response of RC1-RodBCs and RPC1-RodBCs to the photocurrent inputs. Each RC1-RodBC receives photocurrent input from 30 rod photoreceptors, as RC1 database does not include the outer plexiform layer. In the case of RPC1-RodBCs, the number and locations of their synapses with rod photoreceptors are cloned from RPC1. Note that some of the photoreceptors of RPC1 could not be classified between rod and cone photoreceptors. In order to consider the best-case scenario, these indeterminate photoreceptors are assumed to be rod photoreceptors in this work. The number of rod photoreceptor inputs (including indeterminate photoreceptors) per RPC1-RodBC varies between 1 and 7. The photocurrent stimulus with 40 pA peak is applied at each rod photoreceptor connected to the RodBC. The resulting membrane potential at the soma and distant axon terminal of RodBCs are computed and presented in Fig 3. Panel (a)-(d) correspond to RC1-RodBCs and panel (e)-(h) correspond to RPC1-RodBCs. Fig 3(b) and (d) show the response of two RC1-RodBCs (Cell ID: 519 and 5017), each with 30 rod photoreceptor inputs; Whereas, Fig 3(f) and (h) illustrate the response of two RPC1-RodBCs (Cell ID: 822 and 1069) with 7 and 1 rod photoreceptor inputs, respectively. RodBC morphologies along with the locations and number of rod photoreceptors (shown in green color) are provided on the left of each plot. The membrane potential at RodBCs exhibit depolarizing response: first a peak is observed, followed by a plateau, and finally the potential returns to the resting potential. The shape of the membrane potential response is similar for RodBCs from both RC1 and RPC1; however, the magnitude of depolarization varies. For all RC1-RodBCs, the peak membrane potential (Vm_{max}) is found to be approximately -16 mV; in contrast, the peak membrane potential of RPC1-RodBCs varies between -35 mV to -25 mV. For both RPC1-RodBCs and RC1-RodBCs, the membrane potential is higher at the soma and lower at the axon terminal.

4.1 Response to Photocurrent Input

4.1.1 Effect of Locations of Synapses

As the exact locations of the synapses from rod photoreceptors to RodBCs are not available in RC1, we examined how the locations of synapses impact the response of RC1-RodBCs. For each RC1-RodBC, we simulated ten sets of random synapse locations for the 30 rod photoreceptor inputs and observed the resulting membrane potential response. The shape of the membrane potential was found to be similar for all simulation sets. Additionally, for each RC1-RodBC, the peak membrane potential is found to be approximately the same (with a maximum variation of 1 mV) across all simulation sets. Fig 4 summarizes the peak membrane potential of all sets for each RC1-RodBC in box plots with median, lower/upper quartile, and minimum/maximum values. These results suggest that even though the real locations of the synapses are not known, the results of the RC1-RodBCs are not significantly dependent upon the exact locations of the rod photoreceptor inputs. Note that for RC1-RodBCs, the 30 rod photoreceptor inputs are not widely spaced and therefore the randomly generated locations do not differ drastically. However, if the number of rod photoreceptor inputs is much lower (as is the case for RPC1-RodBCs), then the location of the rod photoreceptor inputs would potentially have a more substantial impact on the membrane response of the RodBCs.

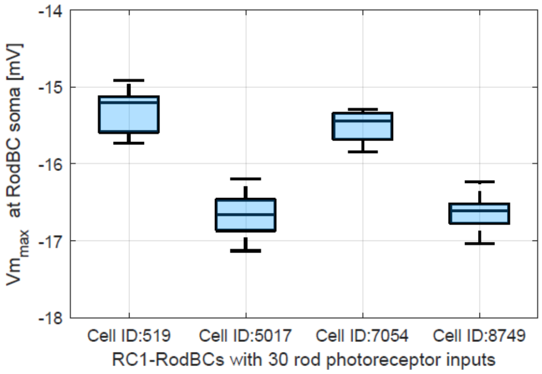

Figure 4: Effect of the locations of rod photoreceptors inputs on RC1-RodBCs response. For each RC1-RodBC, ten sets of random synapse locations for the 30 rod photoreceptor inputs are simulated. The box plots present median, lower/upper quartile, and minimum/maximum values of peak membrane potential at the soma of each RC1-RodBC.

4.1.2 Effect of Number of Rod Photoreceptor Inputs

For all RodBCs (of both volumes), the photocurrent response is similar, except for the difference in the magnitude of the membrane potential. We analyzed the impact of the number of rod photoreceptor inputs per RodBC on the observed differences in membrane potentials of RodBCs. Fig 5 presents the peak membrane potential with respect to the number of rod photoreceptor inputs. Blue filled circles represent RPC1-RodBCs whereas unfilled circles represent RC1-RodBCs. For all RC1-RodBCs, the number of rod photoreceptor inputs to each RodBC is fixed at 30, and the peak membrane potential is approximately -16 mV. In contrast, for RPC1-RodBCs, the number of rod photoreceptor inputs varies from 1 to 7, and peak membrane potential varies from -35 to -25 mV. Cells that receive a higher number of rod photoreceptor inputs show a higher level of depolarization and higher peak membrane potential.

To investigate the lower peak membrane potentials in RPC1-RodBCs and determine if it is due to differences in rod photoreceptor input only, we simulated RC1-RodBCs with a lower number of rod photoreceptor inputs, as is seen in RPC1-RodBCs. This question was explored by simulating all four RC1-RodBCs with 1 to 7 rod photoreceptor inputs (resulting in 28 simulations) and comparing the simulated response with the simulated response from the eight RPC1-RodBCs. The simulated peak membrane potential of these cells is depicted in Fig 6. The results suggest that a lower membrane potential can occur, even in the case of RC1-RodBCs, when fewer rod photoreceptor inputs are provided. The resulting membrane potentials of RC1-RodBCs are not substantially different from RPC1-RodBCs when the same number of rod photoreceptor inputs are provided, despite the morphological differences observed for RPC1-RodBCs. The maximum variation is found for RPC1-RodBC (Cell ID: 1232) and RC1-RodBC (Cell ID: 8749) with 3 rod photoreceptor inputs, which is 2.5 mV. These results suggest that the altered morphology of RPC1-RodBCs, at least early in retinal degeneration, does not play a significant role in changing the response to photocurrent input. Another observation is that for all RC1-RodBCs, the response to photocurrent does not vary linearly with the number of rod photoreceptor inputs.

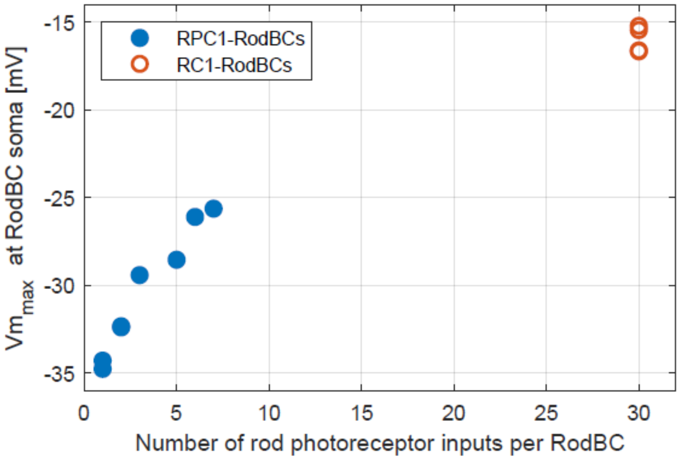

Figure 5: Effect of the number of rod photoreceptor inputs on RodBCs response. RPC1-RodBCs receive input form number of rod photoreceptors between from 1 to 7. Whereas, each RC1-RodBC receive input from 30 rod photoreceptors.

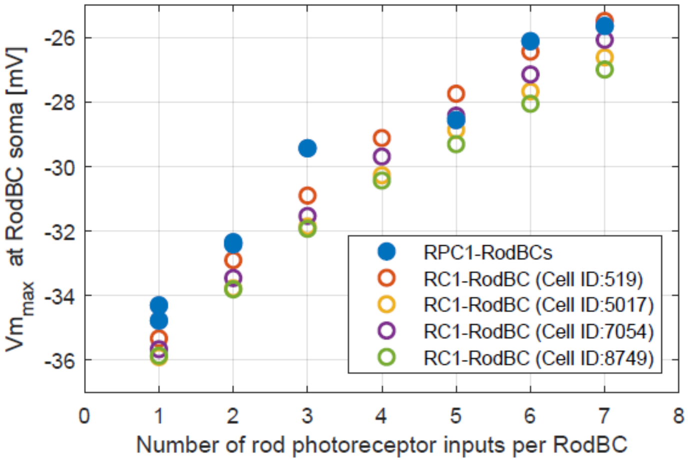

Figure 6: Comparing RC1-RodBCs and RPC1-RodBCs when number of rod photoreceptor inputs to RC1-RodBCs are reduced to those numbers as seen in the case of RPC1-RodBCs. RPC1-RodBCs are simulated with their actual number (according to connectome data) of rod photoreceptor inputs. Whereas, number of rod photoreceptors for each RC1-RodBCs are varied from 1 to 7.

4.2 Frequency Response

Next, we performed frequency response analyses to investigate the differences between RodBCs from the healthy and early-stage degenerated retina. Instead of the photocurrent waveform of the previous section, a sinusoidal input with a frequency range from 0.5 Hz to 100 Hz was used to stimulate the model rod photoreceptors. For this study, we considered one RC1-RodBC (Cell ID: 519) and two RPC1-RodBCs: one cell (Cell ID: 822) with 7 rod photoreceptor inputs and another cell (Cell ID: 1069) with 1 input. The simulated membrane potential and attenuation (in dB) were computed at the soma and distant axon terminal. The results of this frequency analysis are presented in Fig 7. RC1-RodBCs behave as a low pass filter, with 3 dB bandwidth of ≈ 8.9 Hz (see Fig 7(a)), similar to some types of ON-type ConeBCs as reported in [Ichinose, et al., 2014, Ichinose, et al., 2016]. RPC1-RodBCs exhibit low pass filtering, similar to RC1-RodBCs. However, RPC1-RodBC (Cell ID: 822) with 7 rod photoreceptor inputs shows 9.8 dB higher attenuation and RPC1-RodBC (Cell ID: 1069) with 1 rod photoreceptor input shows greater than 24.8 dB higher attenuation compared to RC1-RodBCs. To investigate the impact of fewer rod photoreceptor inputs, we performed frequency analysis on RC1-RodBC (Cell ID: 519) having the same number of rod photoreceptor inputs as RPC1-RodBCs (Cell IDs: 822 and 1069). As shown in Fig 7(b) and 7(c), attenuation at the soma of the RPC1-RodBC is mostly similar to that of the RC1-RodBC with the same number of rod photoreceptor inputs. Even though the same number of rod photoreceptor inputs are connected to each cell, the slight difference in the attenuation at the soma arises due to the difference in the dendritic arbor length and the exact locations of the rod photoreceptor inputs. The attenuation at the axon is higher in the RPC1-RodBC compared to the attenuation at the axon of the RC1-RodBC with the same number of rod photoreceptor inputs. This is most likely due to longer axonal branches of the RPC1-RodBC. The RC1-RodBC with 7 rod photoreceptor inputs shows around 9.9 dB more attenuation than the RC1-RodBC with 30 rod photoreceptor inputs. In contrast, the RC1-RodBC with 1 rod photoreceptor input shows 26.7 dB more attenuation compared to the same RC1-RodBC with 30 rod photoreceptor inputs.

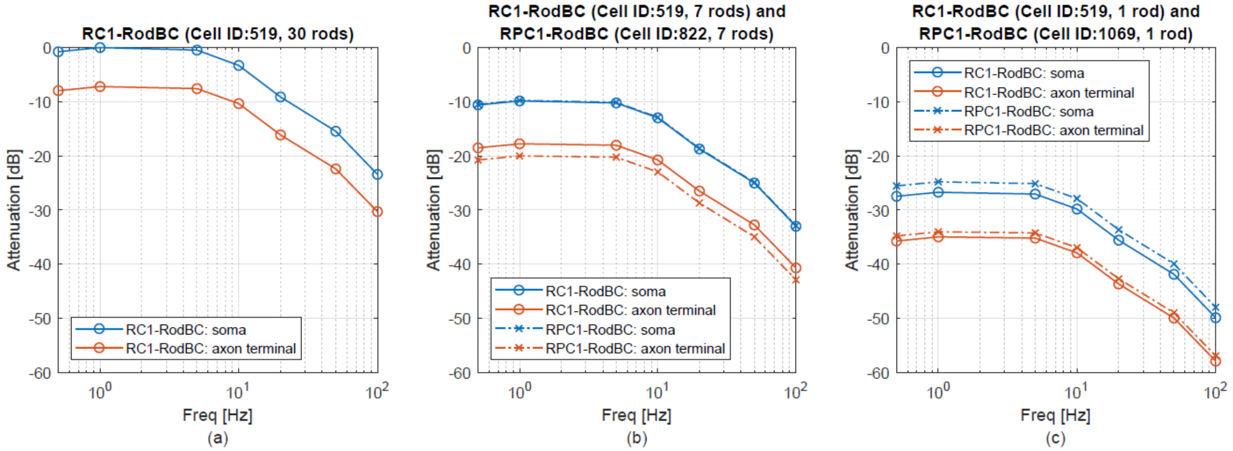

(a) (b) (c)

Figure 7: Frequency response of RC1-RodBCs vs. RPC1-RodBCs. Panel (a) presents frequency response of a RC1-RodBC (Cell ID: 519) with 30 rod photoreceptor inputs. Panel (b) and (c) represent frequency response of RPC1-RodBCs (Cell IDs: 822 and 1069) which receive 7 and 1 rod photoreceptor inputs, respectively. For comparison with RC1-RodBCs, panel (b) and (c) also show frequency response of a RC1-RodBC (Cell ID: 519) with reduced number of rod photoreceptor inputs (7 and 1, respectively).

4.3 Step Input Response

It has been shown that some types of ConeBCs show sustained response to step input, while other types exhibit transient response [Ichinose, et al., 2014, Ichinose, et al., 2016]. To examine the response of RodBCs from the RC1 and RPC1 volumes to the step input, we injected the simulated step photocurrent with 2 s of on time to all rod photoreceptors. All RPC1-RodBCs and RC1-RodBCs showed a sustained response to the step input. Examples of a RC1-RodBC (Cell ID: 519) and two RPC1-RodBCs (Cell IDs: 822 and 1069) are presented in Fig 8. RPC1-RodBCs consistently show lower membrane potentials than that of RC1-RodBCs with 30 rod photoreceptor inputs. Similar to the frequency analysis results, the RC1-RodBC with the same number of rod photoreceptor inputs as the RPC1-RodBC shows a similar response, other than a relatively larger drop in membrane potential at the axon terminals.

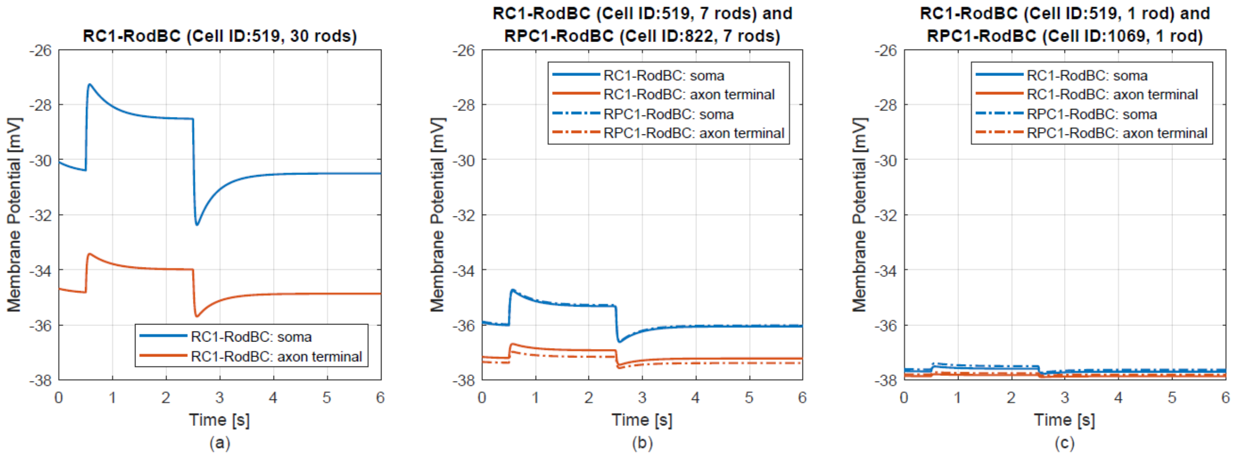

(a) (b) (c)

Figure 8: Step input response of RC1-RodBCs vs. RPC1-RodBCs. Panel (a) displays step input response of a RC1-RodBC (Cell ID: 519) with 30 rod photoreceptor inputs. Panel (b) and (c) show step input response of RPC1-RodBCs (Cell IDs: 822 and 1069) which synapse with 7 and 1 rod photoreceptors, respectively. In order to compare with RC1-RodBCs, panel (b) and (c) also show step input response of a RC1-RodBC (Cell ID: 519) with 7 and 1 rod photoreceptor inputs, respectively.

5. Discussion

We developed connectome-based computational models of current flow from rod photoreceptors to RodBCs in the healthy and early-stage degenerated retina. Our models of RodBCs are based on exact morphology and synaptic information extracted from RC1 and RPC1 connectomes. We have made two assumptions in these computational models. First, we have assumed that the biophysics of the cells in degenerated tissue is the same as that of healthy tissue. We could not tune the model parameters specifically for RPC1-RodBCs due to the lack of experimental recordings from RodBCs in degenerating retinas in the literature. Secondly, the synapse model is the same for both degenerated and healthy retina. This assumption is justified by the fact that synaptic structures, such as ribbon synapses and postsynaptic densities, are found to be similar in both RC1 and RPC1 [Pfeiffer, et al., 2020b]. This is not the case for later stages of retinal degeneration. Further, a recent work on electrical stimulation of ON-type ConeBCs and RodBCs demonstrated that the degenerated bipolar cells responded similar to the healthy bipolar cells and retinal degeneration does not increase stimulation thresholds in bipolar cells [Walston, et al., 2018].

The results of this paper imply that the individual response of RodBCs does not differ substantially in healthy vs. early-stage degenerated retina, with significant differences arising primarily from the different number of photoreceptors present in each case. Even though individual cell responses of RC1-RodBCs and RPC1-RodBCs exhibit insignificant differences, there is still insufficient network data to determine whether these may have a significant aggregated effect at the ganglion cells of the retinal network. From the point of view of therapeutic devices, however, the finding that RodBCs appear to not be affected significantly in the case of early-stage degeneration implies that prosthetic solutions aiming at replacing the functionality of photoreceptors could be highly effective in the early stages of retinal degeneration diseases.

We have previously described that some RPC1-RodBCs have their dendritic arbors reaching to cone photoreceptor terminals [Pfeiffer, et al., 2020b, Pfeiffer, et al., 2020c]. In future work, we plan to include the impact of the observed cone photoreceptor inputs to the membrane potential of RPC1-RodBCs in our model and investigate how that impacts the retinal network of RPC1. Further, as we continue to annotate the inner layer cells of RPC1, these expanded networks will be included in our computational models representing more complete pathways and networks of the healthy and degenerated retina. As further pathoconnectomes become available from our efforts, models will be constructed from these pathoconnectomes as well to represent the various stages of degenerated retina.

6. Conclusions

Understanding changes in the degenerated retina during progression of the disease is crucial for designing effective therapeutic solutions. In this work, we compared the current flow from rod photoreceptors to RodBCs in healthy and early-stage degenerated retina, utilizing retinal connectomes to construct realistic models of RodBCs and their synapses with rod photoreceptors. We implemented the biophysical behavior of the cells and synapses using conductance-based models. Our results suggest that the functional behavior of degenerated RodBCs, in the earliest stages of retinal degeneration, is not significantly different than those in the healthy RodBCs with similar input levels. However, RodBCs in early-stage degenerated retina collect input from fewer numbers of rod photoreceptors in comparison with healthy retina; consequently, RodBCs of the degenerated retina show lower membrane potentials than those of the healthy retina. Frequency response analysis suggests RodBCs in both healthy and degenerated retinas exhibit similar low pass filtering behavior, though there is substantial reduction in frequency-dependent impedances.

Appendix

The values of parameters of rod photoreceptors, RodBCs, and their synapse models are presented in Table 1 and Table 2.

Table 1: Parameters of ionic channel models of rod photoreceptor and RodBC:

Ionic channel	**Rod photoreceptor**		**RodBC**	
	g_{max} **[S/cm^2]**	e **[mV]**	g_{max} **[S/cm^2]**	e **[mV]**
I_{leak}	2.6	-74	7.7	-41
I_h	12.5	-32	31.1	-17.7
I_{Kx}	4.25	-74	-	-
I_{Kv}	50	-80	0.318	-58
I_A	-	-	5.6	-58
I_{Ca}	5	-	2	-
$I_{Cl(Ca)}$	6.5	-20	-	-
$I_{K(Ca)}$	25	-80	1.4	-58

Table 2: Parameters of synapse model:

g_{max} **[S/cm^2]**	e **[mV]**	τ **[ms]**	V_{slope} **[mV]**
2.56	-45	10	10

Acknowledgements:

This work was supported by the National Institutes of Health (NIH) under Grants 1R21EY028744, RO1 EY015128, RO1 EY028927, P30 EY014800 and an Unrestricted Research Grant from Research to Prevent Blindness, New York, NY to the Department of Ophthalmology and Visual Sciences, University of Utah.

References

1. H. Kolb, “How the retina works: Much of the construction of an image takes place in the retina itself through the use of specialized neural circuits,” *American scientist*, vol. 91, no. 1, pp. 28–35, 2003.
2. S. A. Bloomfield and R. F. Dacheux, “Rod vision: pathways and processing in the mammalian retina,” *Progress in retinal and eye research*, vol. 20, no. 3, pp. 351–384, 2001.

3. R. L. Pfeiffer, R. E. Marc, and B. W. Jones, “Persistent remodeling and neurodegeneration in late-stage retinal degeneration,” *Progress in retinal and eye research*, vol. 74, p. 100771, 2020a.
4. R. E. Marc, B. W. Jones, J. R. Anderson, K. Kinard, D. W. Marshak, J. H. Wilson, T. Wensel, and R. J. Lucas, “Neural reprogramming in retinal degeneration,” *Investigative ophthalmology & visual science*, vol. 48, no. 7, pp. 3364–3371, 2007.
5. B. Jones, M. Kondo, H. Terasaki, Y. Lin, M. McCall, and R. Marc, “Retinal remodeling,” *Japanese journal of ophthalmology*, vol. 56, no. 4, pp. 289–306, 2012.
6. R. L. Pfeiffer, J. R. Anderson, J. Dahal, J. C. Garcia, J.-H. Yang, C. L. Sigulinsky, K. Rapp, D. P. Emrich, C. B. Watt, H. Morrison *et al.*, “A pathoconnectome of early neurodegeneration,” *bioRxiv*, 2020b.
7. S. Trenholm and G. B. Awatramani, “Origins of spontaneous activity in the degenerating retina,” *Frontiers in cellular neuroscience*, vol. 9, p. 277, 2015.
8. E. Ivanova, C. W. Yee, R. Baldoni Jr, and B. T. Sagdullaev, “Aberrant activity in retinal degeneration impairs central visual processing and relies on cx36-containing gap junctions,” *Experimental eye research*, vol. 150, pp. 81–89, 2016.
9. J. D. Weiland and M. S. Humayun, “Retinal prosthesis,” *IEEE Transactions on Biomedical Engineering*, vol. 61, no. 5, pp. 1412–1424, 2014.
10. Farnum and G. Pelled, “New vision for visual prostheses,” *Frontiers in Neuroscience*, vol. 14, p. 36, 2020.
11. S. Niketeghad and N. Pouratian, “Brain machine interfaces for vision restoration: the current state of cortical visual prosthetics,” *Neurotherapeutics*, vol. 16, no. 1, pp. 134–143, 2019.
12. P. Kosta, J. Paknahad, E. S. G. Rodríguez, K. Loizos, A. Roy, N. Talbot, S. Seidman, P. Datta, R. Dai, B. Pollack *et al.*, “Electromagnetic safety assessment of a cortical implant for vision restoration,” *IEEE Journal of Electromagnetics, RF and Microwaves in Medicine and Biology*, vol. 2, no. 1, pp. 56–63, 2018.
13. P. R. Troyk, “The intracortical visual prosthesis project,” in *Artificial Vision*. Springer, pp. 203–214, 2017.
14. E. Fernandez and R. A. Normann, “Cortivis approach for an intracortical visual prostheses,” in *Artificial Vision*. Springer, pp. 191–201, 2017.
15. J. Lowery, J. V. Rosenfeld, M. G. Rosa, E. Brunton, R. Rajan, C. Mann, M. Armstrong, A. Mohan, H. Josh, L. Kleeman *et al.*, “Monash vision group’s gennaris cortical implant for vision restoration,” in *Artificial Vision*. Springer, pp. 215–225, 2017.
16. Ahuja, J. Yeoh, J. Dorn, A. Caspi, V. Wuyyuru, M. McMahon, M. Humayun, R. Greenberg, A. I. S. Group *et al.*, “Factors affecting perceptual threshold in argus ii retinal prosthesis subjects,” *Translational vision science & technology*, vol. 2, no. 4, pp. 1–1, 2013.
17. L. N. Ayton, P. J. Blamey, R. H. Guymer, C. D. Luu, D. A. Nayagam, N. C. Sinclair, M. N. Shivdasani, J. Yeoh, M. F. McCombe, R. J. Briggs *et al.*, “First-in-human trial of a novel suprachoroidal retinal prosthesis,” *PloS one*, vol. 9, no. 12, p. e115239, 2014.
18. T. Guo, D. Tsai, S. Bai, J. W. Morley, G. J. Suaning, N. H. Lovell, and S. Dokos, “Understanding the retina: A review of computational models of the retina from the single cell to the network level,” *Critical Reviews^{TM} in Biomedical Engineering*, vol. 42, no. 5, 2014.
19. S. Usui, A. Ishihaiza, Y. Kamiyama, and H. Ishii, “Ionic current model of bipolar cells in the lower vertebrate retina,” *Vision research*, vol. 36, no. 24, pp. 4069–4076, 1996.
20. R. Publio, R. F. Oliveira, and A. C. Roque, “A computational study on the role of gap junctions and rod I_h conductance in the enhancement of the dynamic range of the retina,” *PLoS One*, vol. 4, no. 9, p. e6970, 2009.
21. J. F. Fohlmeister, E. D. Cohen, and E. A. Newman, “Mechanisms and distribution of ion channels in retinal ganglion cells: using temperature as an independent variable,” *Journal of neurophysiology*, vol. 103, no. 3, pp. 1357–1374, 2010.
22. M. Abramian, N. H. Lovell, A. Habib, J. W. Morley, G. J. Suaning, and S. Dokos, “Quasi-monopolar electrical stimulation of the retina: a computational modelling study,” *Journal of neural engineering*, vol. 11, no. 2, p. 025002, 2014.
23. S. Shah and M. D. Levine, “Visual information processing in primate cone pathways. I. A model,” *IEEE Transactions on Systems, Man, and Cybernetics, Part B (Cybernetics)*, vol. 26, no. 2, pp. 259–274, 1996.
24. T. Guo, D. Tsai, S. Sovilj, J. W. Morley, G. J. Suaning, N. H. Lovell, and S. Dokos, “Influence of active dendrites on firing patterns in a retinal ganglion cell model,” in *2013 35th Annual International Conference of the IEEE Engineering in Medicine and Biology Society (EMBC)*, pp. 4557–4560, 2013.

25. K. Loizos, G. Lazzi, J. S. Lauritzen, J. Anderson, B. W. Jones, and R. Marc, “A multi-scale computational model for the study of retinal prosthetic stimulation,” in *2014 36th Annual International Conference of the IEEE Engineering in Medicine and Biology Society (EMBC)*, pp. 6100–6103, 2014.
26. K. Loizos, R. Marc, M. Humayun, J. R. Anderson, B. W. Jones, and G. Lazzi, “Increasing electrical stimulation efficacy in degenerated retina: stimulus waveform design in a multiscale computational model,” *IEEE Transactions on Neural Systems and Rehabilitation Engineering*, vol. 26, no. 6, pp. 1111–1120, 2018.
27. J. Stang, G. Chen, P. Kosta, J. Paknahad, M. Machnoor, E. Iseri, J. Du, D. Brizi, K. Loizos, and G. Lazzi, “Recent advances in computational and experimental bioelectromagnetics for neuroprosthetics,” in International Conference on Electromagnetics in Advanced Applications (ICEAA), pp. 1382–1382, 2019.
28. P. Kosta, K. Loizos, and G. Lazzi, “Stimulus waveform design for decreasing charge and increasing stimulation selectivity in retinal prostheses,” *Healthcare Technology Letters*, vol. 7, no. 3, pp. 66–71, 2020.
29. J. Paknahad, K. Loizos, M. Humayun, and G. Lazzi, “Responsiveness of retinal ganglion cells through frequency modulation of electrical stimulation: A computational modeling study,” in *2020 42nd Annual International Conference of the IEEE Engineering in Medicine & Biology Society (EMBC),* pp. 3393–3398, 2020a.
30. J. Paknahad, K. Loizos, M. Humayun, and G. Lazzi, “Targeted Stimulation of Retinal Ganglion Cells in Epiretinal Prostheses: A Multiscale Computational Study,” *to appear in IEEE Transactions on Neural Systems and Rehabilitation Engineering*, 2020b.
31. J. R. Anderson, B. W. Jones, C. B. Watt, M. V. Shaw, J.-H. Yang, D. DeMill, J. S. Lauritzen, Y. Lin, K. D. Rapp, D. Mastronarde *et al.*, “Exploring the retinal connectome,” *Molecular vision*, vol. 17, p. 355, 2011a.
32. R. E. Marc, B. W. Jones, C. B. Watt, J. R. Anderson, C. Sigulinsky, and S. Lauritzen, “Retinal connectomics: towards complete, accurate networks,” *Progress in retinal and eye research*, vol. 37, pp. 141–162, 2013.
33. R. L. Pfeiffer, J. R. Anderson, J. Dahal, J. C. Garcia, J.-H. Yang, C. L. Sigulinsky, K. Rapp, D. P. Emrich, C. B. Watt, H. Morrison, A. R. Houser, R. E. Marc, and B. W. Jones, “A pathoconnectome of early neurodegeneration: Network changes in retinal degeneration.” *Experimental eye research*, p. 108196, 2020c.
34. L. Hodgkin and A. F. Huxley, “A quantitative description of membrane current and its application to conduction and excitation in nerve,” *The Journal of physiology*, vol. 117, no. 4, p. 500, 1952.
35. M. L. Hines and N. T. Carnevale, “The neuron simulation environment,” *Neural computation*, vol. 9, no. 6, pp. 1179–1209, 1997.
36. J. R. Anderson, S. Mohammed, B. Grimm, B. W. Jones, P. Koshevoy, T. Tasdizen, R. Whitaker, and R. E. Marc, “The viking viewer for connectomics: scalable multi-user annotation and summarization of large volume data sets,” *Journal of microscopy*, vol. 241, no. 1, pp. 13–28, 2011b.
37. D. Auber, “Tulip—a huge graph visualization framework,” in *Graph drawing software*. Springer, pp. 105–126, 2004.
38. E. Kerzner, A. Lex, C. L. Sigulinsky, T. Urness, B. W. Jones, R. E. Marc, and M. Meyer, “Graffinity: Visualizing connectivity in large graphs,” in *Computer Graphics Forum*, vol. 36, no. 3. Wiley Online Library, pp. 251–260, 2017.
39. R. L. Pfeiffer, J. R. Anderson, D. P. Emrich, J. Dahal, C. L. Sigulinsky, H. A. Morrison, J.-H. Yang, C. B. Watt, K. D. Rapp, M. Kondo, H. Terasaki, J. C. Garcia, R. E. Marc, and B. W. Jones, “Pathoconnectome analysis of muller cells in early retinal remodeling,” in¨ *Retinal Degenerative Diseases, Advances in Experimental Medicine and Biology*. Springer, vol. 1185, pp. 365–370, 2019.
40. N. Cuenca, I. Pinilla, Y. Sauve, B. Lu, S. Wang, and R. D. Lund, “Regressive and reactive changes in the connectivity patterns of rod and cone pathways´ of p23h transgenic rat retina,” *Neuroscience*, vol. 127, no. 2, pp. 301–317, 2004.
41. Y.-W. Peng, Y. Hao, R. M. Petters, and F. Wong, “Ectopic synaptogenesis in the mammalian retina caused by rod photoreceptor-specific mutations,” *Nature neuroscience*, vol. 3, no. 11, pp. 1121–1127, 2000.
42. H. Peng, A. Bria, Z. Zhou, G. Iannello, and F. Long, “Extensible visualization and analysis for multidimensional images using vaa3d,” *Nature protocols*, vol. 9, no. 1, pp. 193–208, 2014.
43. Behrens, T. Schubert, S. Haverkamp, T. Euler, and P. Berens, “Connectivity map of bipolar cells and photoreceptors in the mouse retina,” *Elife*, vol. 5, p. e20041, 2016.

44. Y. Tsukamoto and N. Omi, “Functional allocation of synaptic contacts in microcircuits from rods via rod bipolar to aii amacrine cells in the mouse retina,” *Journal of Comparative Neurology*, vol. 521, no. 15, pp. 3541–3555, 2013.
45. Y. Kamiyama, T. O’Sura, and S. Usui, “Ionic current model of the vertebrate rod photoreceptor,” *Vision research*, vol. 36, no. 24, pp. 4059–4068, 1996.
46. R. Publio, R. F. Oliveira, and A. C. Roque, “A realistic model of rod photoreceptor for use in a retina network model,” *Neurocomputing*, vol. 69, no. 10-12, pp. 1020–1024, 2006.
47. E. Kourennyi, X.-d. Liu, J. Hart, F. Mahmud, W. H. Baldridge, and S. Barnes, “Reciprocal modulation of calcium dynamics at rod and cone photoreceptor synapses by nitric oxide,” *Journal of neurophysiology*, vol. 92, no. 1, pp. 477–483, 2004.
48. L. Oltedal, M. L. Veruki, and E. Hartveit, “Passive membrane properties and electrotonic signal processing in retinal rod bipolar cells,” *The Journal of physiology*, vol. 587, no. 4, pp. 829–849, 2009.
49. B. Mulloney, “During fictive locomotion, graded synaptic currents drive bursts of impulses in swimmeret motor neurons,” *Journal of Neuroscience*, vol. 23, no. 13, pp. 5953–5962, 2003.
50. M. A. Sikora, J. Gottesman, and R. F. Miller, “A computational model of the ribbon synapse,” *Journal of neuroscience methods*, vol. 145, no. 1-2, pp. 47–61, 2005.
51. B. Trexler, W. Li, and S. C. Massey, “Simultaneous contribution of two rod pathways to aii amacrine and cone bipolar cell light responses,” *Journal of neurophysiology*, vol. 93, no. 3, pp. 1476–1485, 2005.
52. K. Cho, S. Baek, S.-W. Cho, J.-H. Kim, Y. S. Goo, J. K. Eshraghian, N. Iannella, and K. Eshraghian, “Signal flow platform for mapping and simulation of vertebrate retina for sensor systems,” *IEEE Sensors Journal*, vol. 16, no. 15, pp. 5856–5866, 2016.
53. T. Ichinose, B. Fyk-Kolodziej, and J. Cohn, “Roles of on cone bipolar cell subtypes in temporal coding in the mouse retina,” *Journal of Neuroscience*, vol. 34, no. 26, pp. 8761–8771, 2014.
54. T. Ichinose and C. B. Hellmer, “Differential signalling and glutamate receptor compositions in the off bipolar cell types in the mouse retina,” *The Journal of physiology*, vol. 594, no. 4, pp. 883–894, 2016.
55. S. T. Walston, R. H. Chow, and J. D. Weiland, “Direct measurement of bipolar cell responses to electrical stimulation in wholemount mouse retina,” *Journal of neural engineering*, vol. 15, no. 4, p. 046003, 2018.

Figure Legends

Figure 1: Morphology of healthy (left) and degenerated (right) RodBCs, extracted from RC1 and RPC1, respectively. Cell somas are depicted in blue, dendrites in black, axons in yellow and axon terminals in red color.

Figure 2: Simulated response of rod photoreceptor. Panel (a) presents simulated photocurrent waveforms with various current amplitudes and panel (b) displays the resulting membrane potential at the soma of rod photoreceptor corresponding to the photocurrents of panel (a).

Figure 3: Simulated response of RC1-RodBCs vs. RPC1-RodBCs. Panel (a)-(d) correspond to two RC1-RodBCs (Cell IDs: 519 and 5017), whereas panel (e)-(h) correspond to two RPC1-RodBCs (Cell IDs: 822 and 1069). Locations and number of rod photoreceptor inputs for each RodBC are shown by green color. Panel (b), (d), (f) and (h) present the membrane potential at the somas and distant axon terminals of the RodBCs shown in panel (a), (c), (e) and (g), respectively.

Figure 4: Effect of the locations of rod photoreceptors inputs on RC1-RodBCs response. For each RC1-RodBC, ten sets of random synapse locations for the 30 rod photoreceptor inputs are simulated. The box plots present median, lower/upper quartile, and minimum/maximum values of peak membrane potential at the soma of each RC1-RodBC.

Figure 5: Effect of the number of rod photoreceptor inputs on RodBCs response. RPC1-RodBCs receive input form number of rod photoreceptors between from 1 to 7. Whereas, each RC1-RodBC receive input from 30 rod photoreceptors.

Figure 6: Comparing RC1-RodBCs and RPC1-RodBCs when number of rod photoreceptor inputs to RC1-RodBCs are reduced to those numbers as seen in the case of RPC1-RodBCs. RPC1-RodBCs are simulated with their actual number (according to connectome data) of rod photoreceptor inputs. Whereas, number of rod photoreceptors for each RC1-RodBCs are varied from 1 to 7.

Figure 7: Frequency response of RC1-RodBCs vs. RPC1-RodBCs. Panel (a) presents frequency response of a RC1-RodBC (Cell ID: 519) with 30 rod photoreceptor inputs. Panel (b) and (c) represent frequency response of RPC1-RodBCs (Cell IDs: 822 and 1069) which receive 7 and 1 rod photoreceptor inputs, respectively. For comparison with RC1-RodBCs, panel (b) and (c) also show frequency response of a RC1-RodBC (Cell ID: 519) with reduced number of rod photoreceptor inputs (7 and 1, respectively).

Figure 8: Step input response of RC1-RodBCs vs. RPC1-RodBCs. Panel (a) displays step input response of a RC1-RodBC (Cell ID: 519) with 30 rod photoreceptor inputs. Panel (b) and (c) show step input response of RPC1-RodBCs (Cell IDs: 822 and 1069) which synapse with 7 and 1 rod photoreceptors, respectively. In order to compare with RC1-RodBCs, panel (b) and (c) also show step input response of a RC1-RodBC (Cell ID: 519) with 7 and 1 rod photoreceptor inputs, respectively.

Figure1

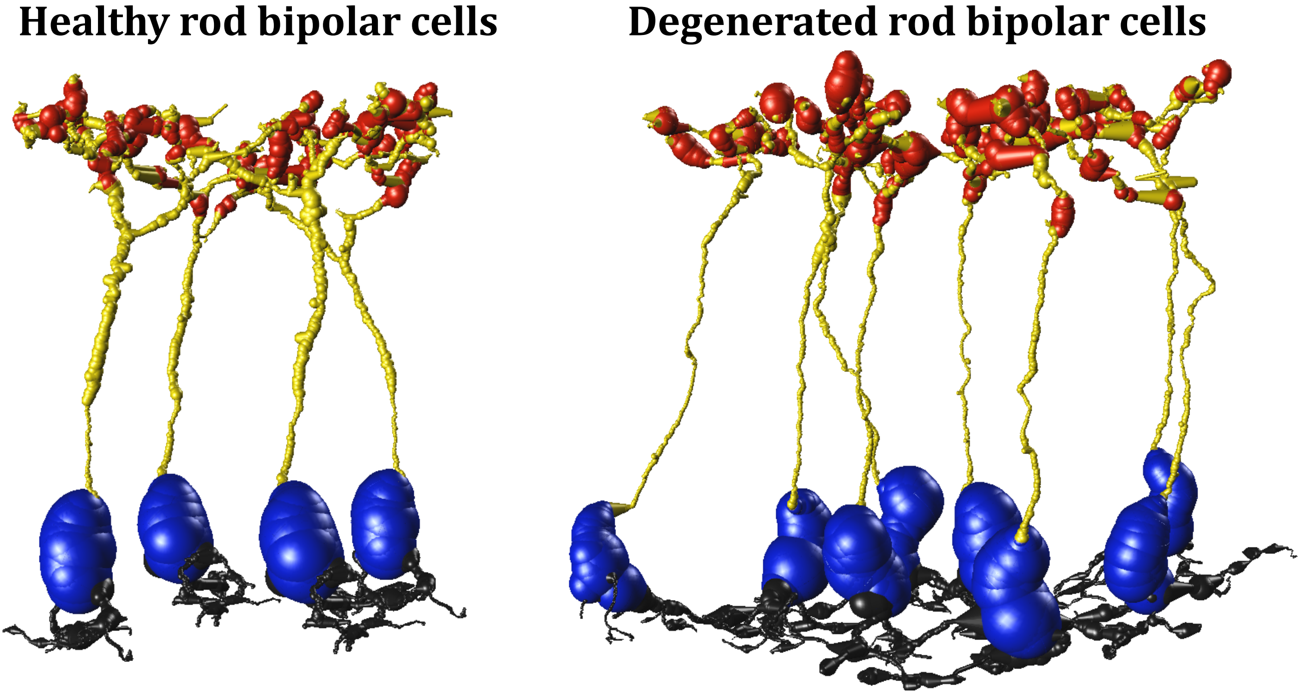

Healthy rod bipolar cells

Degenerated rod bipolar cells

Figure2

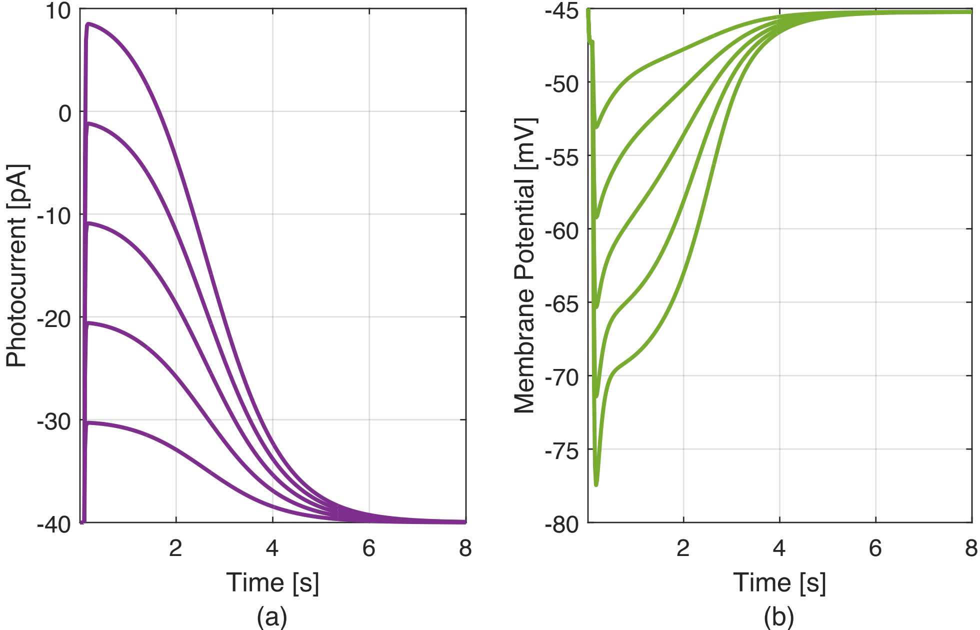
10
0
-10
-20
-30
-40
Photocurrent [pA]
2
4
6
8
Time [s]
(a)
-45
-50
-55
-60
-65
-70
-75
-80
Membrane Potential [mV]
2
4
6
8
Time [s]
(b)

Figure3_abcd

RC1-RodBCs and simulated response

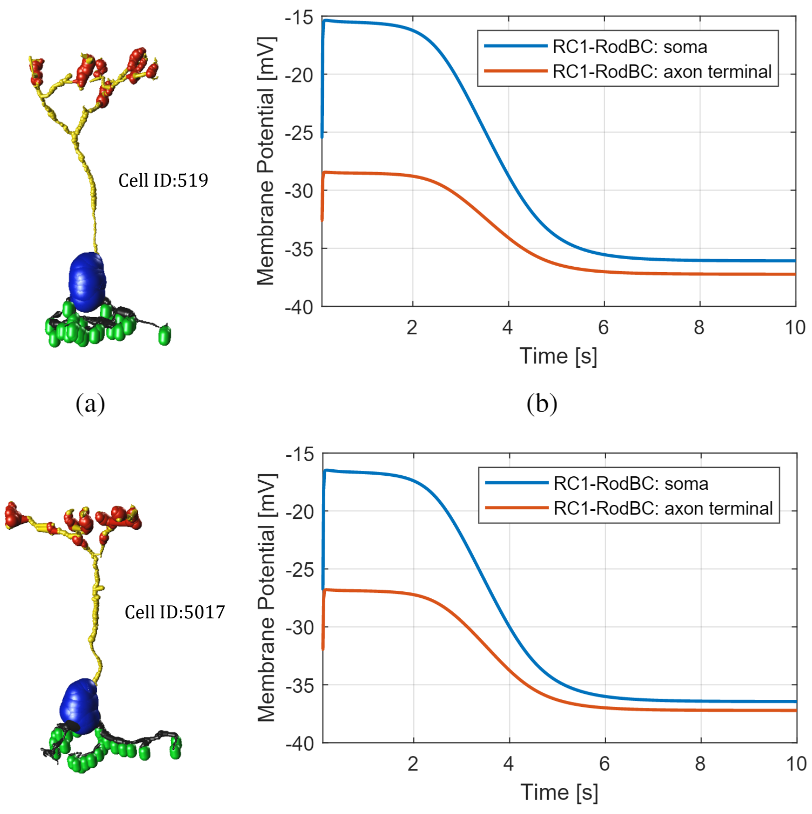

(a) (b)

(c) (d)

Figure3_efgh

RPC1-RodBCs and simulated response

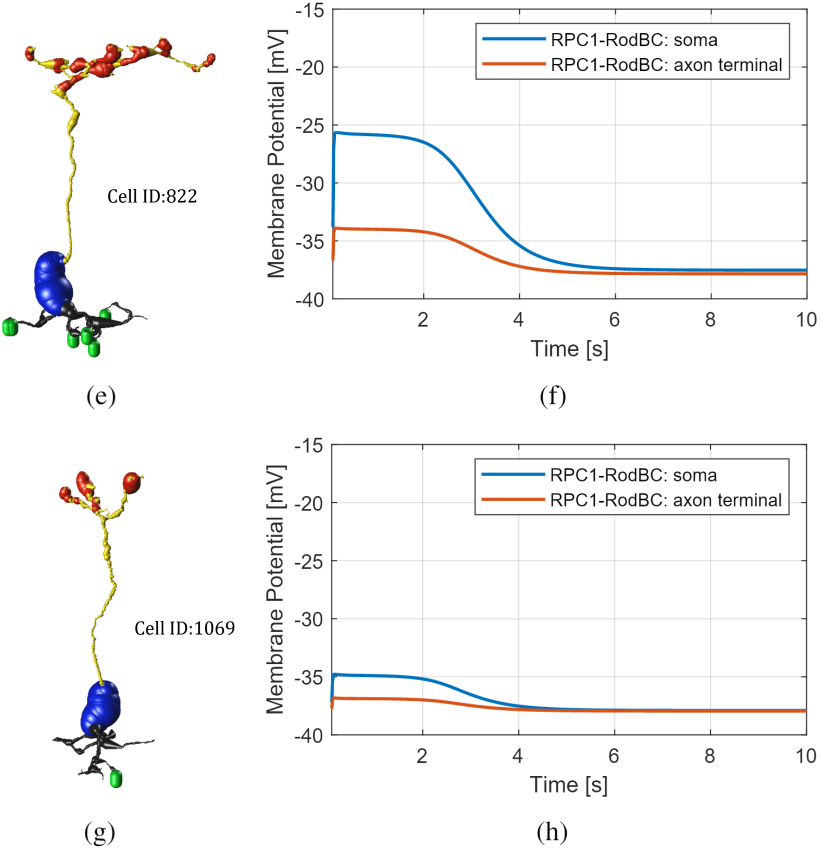

(e) (f)

(g) (h)

Figure4

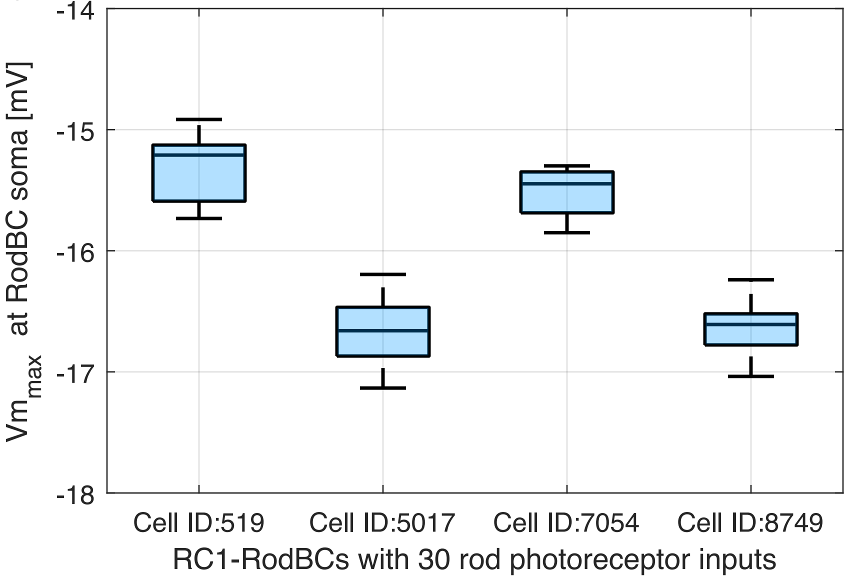
-14
-15
-16
-17
-18
Vm$_{max}$ at RodBC soma [mV]
Cell ID:519
Cell ID:5017
Cell ID:7054
Cell ID:8749
RC1-RodBCs with 30 rod photoreceptor inputs

Figure5

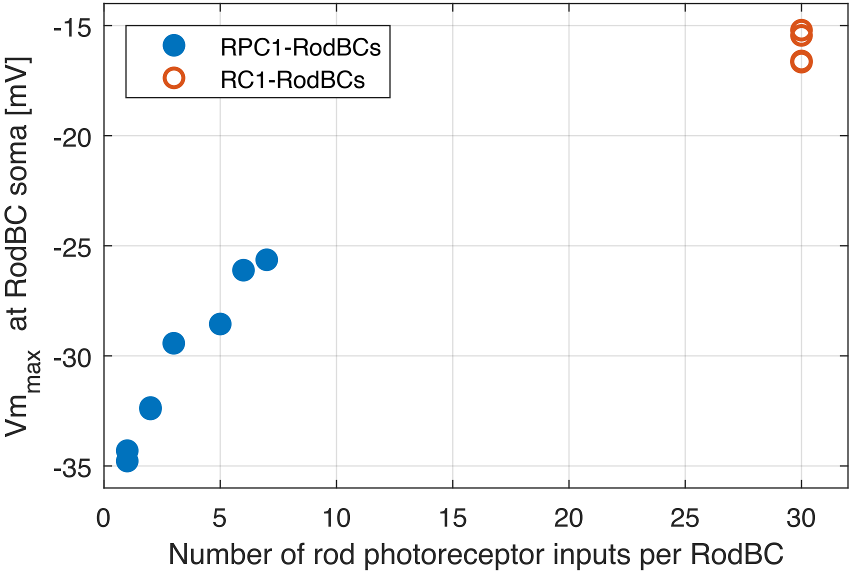

● RPC1-RodBCs
○ RC1-RodBCs
Vm_{max} at RodBC soma [mV]
-15
-20
-25
-30
-35
0
5
10
15
20
25
30
Number of rod photoreceptor inputs per RodBC

Figure6

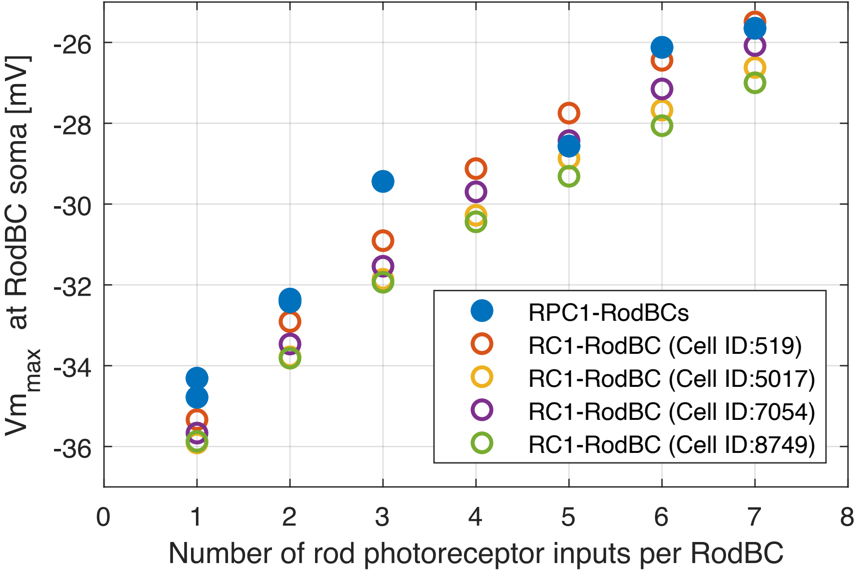

-26
-28
-30
-32
-34
-36
0
1
2
3
4
5
6
7
8
Vm_{max} at RodBC soma [mV]
Number of rod photoreceptor inputs per RodBC
● RPC1-RodBCs
○ RC1-RodBC (Cell ID:519)
○ RC1-RodBC (Cell ID:5017)
○ RC1-RodBC (Cell ID:7054)
○ RC1-RodBC (Cell ID:8749)

Figure7

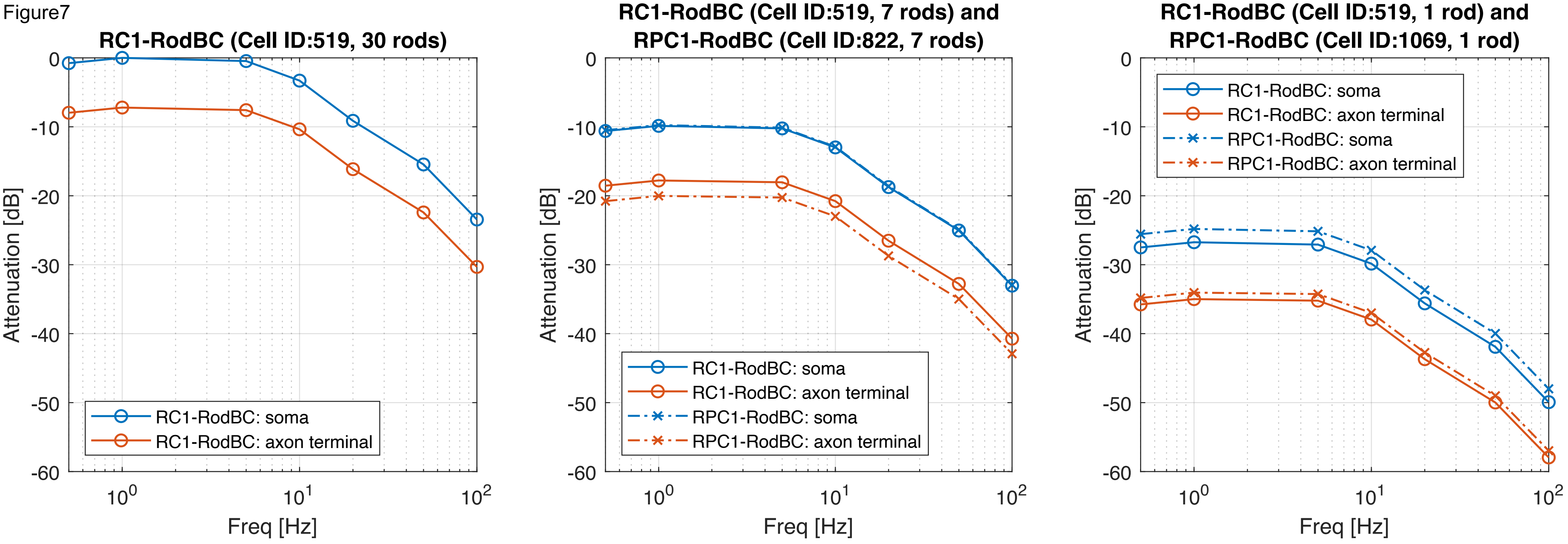

RC1-RodBC (Cell ID:519, 30 rods)
RC1-RodBC: soma
RC1-RodBC: axon terminal
RC1-RodBC (Cell ID:519, 7 rods) and RPC1-RodBC (Cell ID:822, 7 rods)
RC1-RodBC: soma
RC1-RodBC: axon terminal
RPC1-RodBC: soma
RPC1-RodBC: axon terminal
RC1-RodBC (Cell ID:519, 1 rod) and RPC1-RodBC (Cell ID:1069, 1 rod)
RC1-RodBC: soma
RC1-RodBC: axon terminal
RPC1-RodBC: soma
RPC1-RodBC: axon terminal
Attenuation [dB]
0
-10
-20
-30
-40
-50
-60
Freq [Hz]
10^0
10^1
10^2

(a) (b) (c)

Figure8

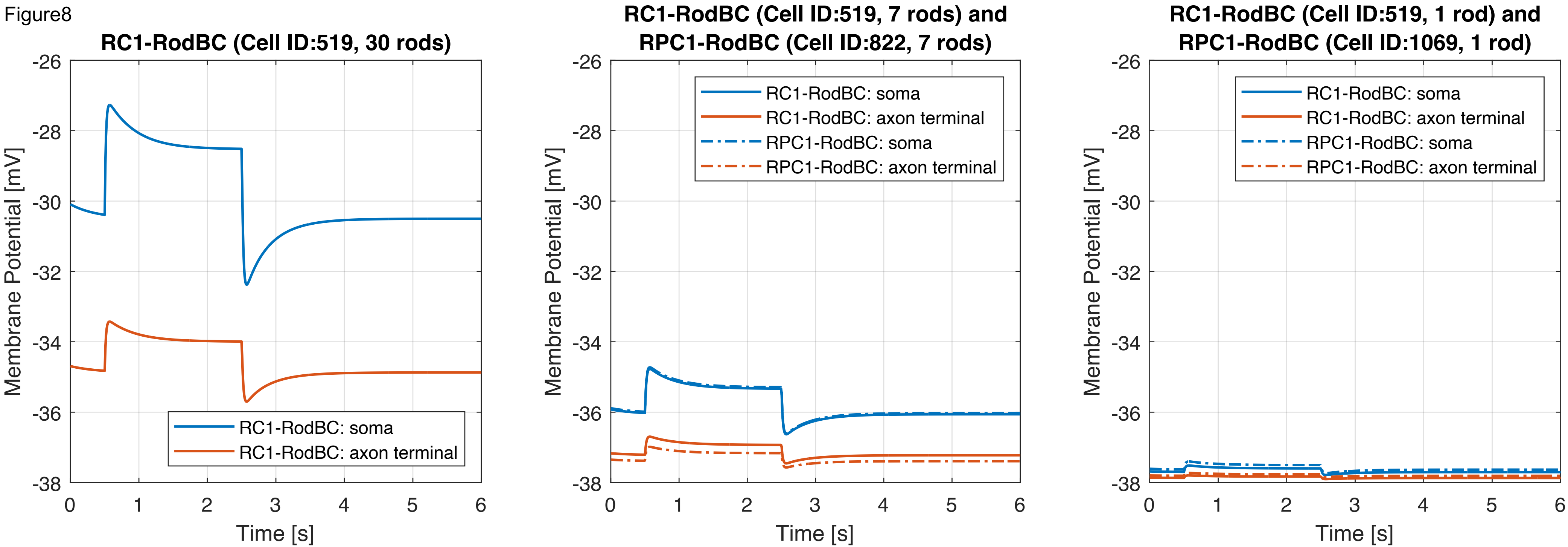
RC1-RodBC (Cell ID:519, 30 rods)
RC1-RodBC (Cell ID:519, 7 rods) and RPC1-RodBC (Cell ID:822, 7 rods)
RC1-RodBC (Cell ID:519, 1 rod) and RPC1-RodBC (Cell ID:1069, 1 rod)
Membrane Potential [mV]
-26
-28
-30
-32
-34
-36
-38
Time [s]
0
1
2
3
4
5
6
RC1-RodBC: soma
RC1-RodBC: axon terminal
RPC1-RodBC: soma
RPC1-RodBC: axon terminal

(a)

(b)

(c)